High resolution density pedestal measurements during edge localized modes by short-pulse reflectometry in the TCV tokamak

P. A. Molina Cabrera [1,2] ‡ **B. Labit**[2]**, S. Coda**[2]**, L. Porte**[2] **, and the TCV team** §

[1]Plasma Science and Fusion Center, Massachusetts Institute of Technology, Cambridge, Massachusetts, United States of America
[2]Ecole Polytechnique Fédérale de Lausanne (EPFL), Swiss Plasma Center (SPC), CH-1015 Lausanne, Switzerland

E-mail: molinaca@mit.edu

Abstract. This publication presents high spatio-temporal resolution (mm/μs) density profile measurements of the pedestal top during type I, III, and small edge localized mode (ELM) H-mode plasmas in the Tokamak à Configuration Variable (TCV). These measurements were performed using a novel short-pulse reflectometer. Average inter-ELM density profiles are obtained via conditional averaging using the D_α trace as ELM indicator. Changes to the pedestal density profile gradients prior to type-III ELMs reveal unique pedestal dynamics leading to the ELM crash which can provide important experimental data for validation of non-linear MHD ELM simulations. The small-ELM scenario is found to feature a $\sim$25-35 kHz quasi-coherent density fluctuation near the separatrix ρ_ψ $\sim$0.993-1.05 not observed during a similar type-I ELM discharge. This oscillation is also found in low-field-side magnetic pick-up probes displaying a ballooning character and n=+1 toroidal mode number. This oscillation could help explain the markedly different pedestal dynamics observed in the small-ELM regime.

Keywords: edge localized mode, reflectometry, tokamak, ELM precursors. Submitted to:

‡ Present address: Max Planck Institute for Plasma Physics. Boltzmannstrasse 2, 85748 Garching, Germany.
§ See authors list of S. Coda et al., 2019, Nucl. Fusion 59 112023

1. Introduction

The thermonuclear research reactor ITER [1] hopes to achieve high fusion gain Q≥5-10 for 300-500 s (where Q is the ratio of fusion power to external heating power) thanks to the successful sustainment of a steady-state H-mode. In H-mode [2], an energy and particle transport barrier develops in the plasma edge thanks to a sheared ExB flow that quenches turbulent fluctuations [3]. The large density and temperature gradients resulting from the decrease in radial transport raise the pressure performance of the core plasma as if put on a 'pedestal'. This pedestal region is usually contained inside $\rho_\psi = 0.95\text{-}1.0$ (where ρ_ψ stands for the normalized poloidal flux function $\rho_\psi = \sqrt{\frac{\psi - \psi_a}{\psi_s - \psi_a}}$ [4] , where ψ, s and a refer to the poloidal flux function, separatrix, and magnetic axis respectively). Although micro-instabilities are quenched by the shear flow, the large pressure gradient in the pedestal region can drive MHD instabilities. The most ubiquitous of these is the edge-localized mode (ELM), which leads to a fast loss of energy and particles from the plasma edge [5][6][7]. ELMs are helpful to maintain a quasi-stationary H-mode by flushing out impurities. However, they are also responsible for a rapid release of plasma energy of roughly 5-10% in sub-ms scales. This energy release can be problematic for future reactor plasma-facing components. If unmitigated, these large type-I ELMs can exceed the maximum peak heat flux allowed by ITER plasma-facing components [8] at $\sim 10\,\mathrm{MW\,m^{-2}}$.

Great progress has been made in predicting the macroscopic stability limits of the pedestal. The EPED model [9], for instance, is capable of predicting pedestal pressure height and width within 20% over a wide range of devices and experimental conditions, but it requires the pedestal top density as an input. A robust and validated model of the underlying physics behind the pedestal density structure is still missing. The complex interplay of divertor conditions, neutral and impurity penetration, as well as electron turbulent transport remain active research topics [10].

Beyond predictions of macroscopic pedestal quantities, a thorough theoretical description of the non-linear phase of the ELM crash has also received recent attention. Both analytical [11] and numerical approaches (i.e. JOREK [12] [13]) are getting closer to describing the non-linear ballooning precursor instabilities behind both ELMs and disruptions. Experimental evidence of various pedestal modes have been reported across many toka-

maks [14]. Non-linear interactions [15] between these modes have been reported and encourage further studies of the subject. A better understanding of the physics of these precursors could lead to improved predictive capabilities and mitigation insights.

High spatio-temporal resolution measurements of plasma density can prove decisive to better understand the physics of the pedestal. This paper presents new measurements of plasma density profiles and fluctuations performed with a broadband short-pulse reflectometer (SPR) [16], recently made operational on the Tokamak à Configuration Variable (TCV) [17]. The instrument can access both equilibrium density profiles and long-wavelength [18] ($k_\perp < 2.6\,\mathrm{cm^{-1}}$, $k_\perp \rho_s < 0.26$, where $k_\perp$ is the wavenumber of fluctuations perpendicular to the main magnetic field and $\rho_s = c_s/\Omega_i$ is the ions sound speed radius, $c_s = \sqrt{T_e/m_i}$ is the ion sound speed, and $\Omega_i = Z_{\mathrm{eff}} e B/m_i$ is the ion cyclotron frequency) density fluctuation information with sub-cm spatial resolution and micro-second time resolution. This publication presents the results of applying this new diagnostic to the study of TCV's density pedestal during three different ELMy H-mode scenarios featuring type-III, type-I, and small ELMs. The type-III ELM scenario addressed here is a diverted ohmic H-mode first presented by Weisen et al. [19] and further studied in [20] and [21]. The type-I and small-ELM regimes were obtained using 1MW of external neutral-beam injection heating and have been addressed in a recent publication by Labit et al. [8] and Sheikh et al. [22]. The small-ELM regime is of great interest to the community since it features confinement properties similar to the type-I ELM scenario but features significantly reduced heat loads to plasma-facing components [8]. The dynamics of pedestal stability during small ELMs is markedly different from that of type-I ELMs described by EPED and remains to be better understood theoretically [23][6] and characterized experimentally. This publication will show that the SPR diagnostic is capable of a detailed characterization of the density pedestal evolution on the ELM time scale (sub ms), and that it holds great potential for model validation.

The article is structured as follows. It begins with an introduction to the SPR diagnostic and data analysis methods in sections 2 and 3, respectively. A description of the experimental scenarios follows in section 4. Average inter-ELM density profile and density gradient evolution for all three scenarios is then presented in section 5. Lastly, inter-ELM density fluctuations are presented in section 6 followed by conclusions.

2. SPR diagnostic description

Reflectometry is an active diagnostic technique capable of inferring density profiles and fluctuations by launching mm-scale electromagnetic waves that encounter opaque (or 'cutoff') layers in high-density tokamak plasmas [24][Ch.4] [25]. Once the density is large enough, the refractive index of these waves approaches zero and the wave is *reflected* back to the antenna for detection. By measuring phase differences or the group-delay - defined as the rate of change of phase with changing frequency $\partial\phi/\partial\omega$ - over frequency, both density profile [26] and fluctuation information [27] can be inferred.

Short pulse reflectometry (SPR) [25], [28] [29] [30] consists of sending broadband pulses ($\sim$1 ns) with a defined carrier frequency and measuring their round-trip group-delay using precise chronometers. SPR is a uniquely attractive approach to reflectometry. First, assuming negligible absorption and weak dispersion, the group-delay of a pulse with a defined carrier frequency can be measured directly. This stands in contrast to continuous-wave frequency modulation (CW-FM) techniques [31] where the linearity of frequency sweep is vital to measure accurate group-delays. Second, pulse propagation through the plasma occurs in the nanosecond-scale, at least 2 orders of magnitude under the typical sub-microsecond turbulence time scales (ion gyrofrequency scale): the plasma can be considered to be truly frozen during pulse propagation. Finally, given the time-domain nature of SPR measurements, spurious reflections in waveguides, vacuum-windows, and in-plasma coherent back-scattering can be separated from the plasma cutoff reflection and easily filtered.

In TCV's SPR, short ($\sim$700 ps) pulses in the V-band (50-75 GHz) are produced by using a fast arbitrary waveform generator (AWG) (25 GHz analog bandwidth) and x6 varactor multipliers. The group-delay of these pulses has been measured down to 17 ps(2.5 mm) resolution using both analog and direct sampling pulse timing techniques against a mirror including 10 dB power variations [16]. The analog timing circuit used in this publication consists of a constant fraction discriminator (CFD), a time-to-amplitude converter (TAC), and an analog to digital converter (ADC). All these elements are found in the commercial SPC-150Nx timing module from Becker and Hickl GmbH [32].

Group-delays from pulses reflected against a plasma cutoff show increased group-delay variations beyond 17 ps, which are quantified through the standard-deviation (σ). L and H-mode plasmas show σs of $\sim$100 and $\sim$20 ps, respectively, both above the diagnostic resolution [16]. Direct digital sampling of reflected pulses allowed the first simultaneous measurement of pulse amplitude, width, and group-delay. Direct digital sampling - performed with a fast (45 GSamp/s, 13 GHz analog bandwidth) oscilloscope - confirmed that while pulse-dispersion does occur in turbulent L-mode plasmas, pulse widths increase only

by 4% on average [16]. Hence, pulse-dispersion can occur [33], but it is not an obstacle to measuring average group-delays with pulse reflectometry. Using the fits from 2700 pulses in an L-mode plasma, a standard-deviation in the pulse width of $\sim$70ps was recorded. Thus, since analog timing circuits are unable to quantify changes to group-delays caused by pulse dispersion, the inherent uncertainty of analog group-delay measurements was increased from 17 to 40 ps in L-mode plasmas [16].

When measuring inside the pedestal of H-mode discharges, group-delay σs are about $\sim$20 ps- only 3 ps above diagnostic limits. Thus, it is believed that very little pulse dispersion takes place in the H-mode pedestal. This is likely due to both the large density gradients and the reduced fluctuation level due to well-documented ExB shearing decorrelation of turbulent eddies [34]. This reduced group-delay σ makes SPR an ideal diagnostic to measure the H-mode pedestal since it features excellent $\sim$20 ps (3 mm) pulse-timing precision. Given the short periods of time ($<$5 ms) that can currently be recorded with the direct digital sampling technique, all data presented here was taken using the analog SPC-150Nx pulse-timing module which allows group-delay measurements of up to 2.4 s at 8.3 MHz pulse repetition rate (PRR).
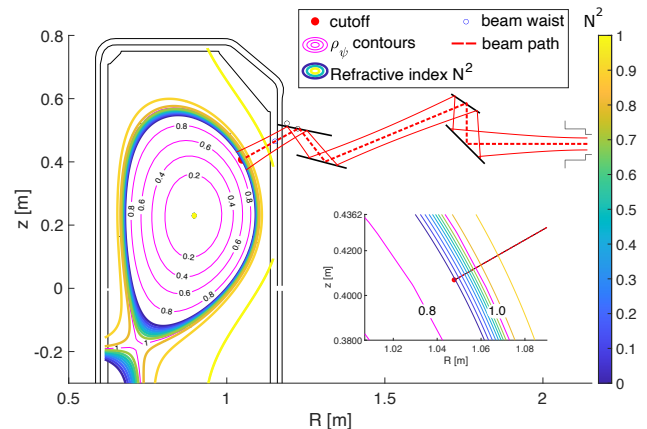

Figure 1. To scale drawing of the upper lateral diagnostic launcher antenna directing a 60 GHz beam towards the H-mode pedestal of discharge 62744 at 0.9 s. Notice the refractive index decreasing towards zero where the cutoff layer (N^2=0) is found.

TCV's SPR diagnostic uses a uniquely flexible quasi-optical launcher antenna system inherited from TCV's second-harmonic electron cyclotron resonance heating (ECRH) launcher antennas [35], shown in figure 1. This antenna allows poloidal (5-50°) and toroidal (-180-180°) steering of the beam with 0.2° accuracy. This launcher system also features a pair of polariser miter bends [36] housed inside an oversized corrugated circular waveguide [37]. The polariser miter bends allow coupling of the diagnostic output beam into either O or X-mode polarisations in a wide range of plasma scenarios [38]. The output polarization freedom allows coverage of 3-7 and

$0.8\text{-}4 \times 10^{19} \, \mathrm{m}^{-3}$ densities in O and X-mode, respectively. Further diagnostic technical details can be found in a recent publication [16].

3. Data analysis procedure

In reflectometry, the plasma electron density can be inferred from measurements of the round-trip group-delay of waves reflected in perpendicular incidence to a cutoff layer over a number of frequencies. In contrast to conventional radar where the pulse group-delay (or time-of-flight) can be trivially transformed into a distance to a target by taking a constant speed of light, in fusion plasmas the refractive index of the wave varies between 1 in vacuum down to 0 at the cutoff layer according to the density profile leading to the cutoff (see figure 1). Thus, inferring density profiles from reflectometry requires information about the plasma density and magnetic field reconstruction leading to the first cutoff layer as well as an inversion algorithm to interpret group-delays as distances from the antenna. In TCV, group-delay initialization is obtained using a 2D ray-tracing code: PrefGeom [38] shown in figure 1. It takes density information from the Thomson-scattering diagnostic and average reciprocating-probe profiles for the scrape-off-layer (SOL) [39]. LIUQE magnetic reconstruction is used to provide magnetic field information through the Psi-toolbox package [40]. These two are combined to obtain two important initialization variables to the inversion algorithm: group-delay curves under the first sampling frequency [26] and the physical location of the cutoff layer of the first frequency - $f_0 = 50\text{GHz}$ in our case. The analytical Abel transform [24, Ch. 4.5] is then used to transform group-delays into physically meaningful distances to cutoff layers:

$$
\begin{aligned}
x_c(\omega) &= a - \frac{c}{\pi} \int_0^\omega \frac{\partial \phi}{\partial \omega'} \frac{d\omega'}{\sqrt{\omega^2 - \omega'^2}} \\
&= a - \frac{c}{\pi} \left(\int_0^{2\pi f_0} \frac{\partial \phi}{\partial \omega'} (\mathrm{PG}) \frac{d\omega'}{\sqrt{\omega^2 - \omega'^2}} \right. \\
&\quad \left. + \int_{2\pi f_0}^\omega \frac{\partial \phi}{\partial \omega'} (\mathrm{SPR}) \frac{d\omega'}{\sqrt{\omega^2 - \omega'^2}} \right)
\end{aligned}
\tag{1}
$$

where PG stands for group delay curves obtained with PrefGeom, f_0 is the first (lowest) reflectometer frequency, x_c is the distance to the cutoff layer, a is the distance from the antenna to the start of the plasma, ω is the angular frequency, ω' is the angular frequency integration variable, and ϕ is the phase.

TCV's SPR diagnostic undergoes an independent calibration procedure to ensure group-delay changes over frequency are exclusively due to the plasma density profile. Firstly, group-delay variations over frequency produced by mm-wave and transmission-line hardware are eliminated by obtaining a common group-delay from a mirror at the entrance of the launcher antenna. Secondly, variations of group-delay over frequency due to the quartz vacuum window at the entrance of the launcher antenna are applied to the data *a posteriori* based on VNA [30, ap. 1](vector network analyzer) measurements of the window properties.

SPR raw group-delay data acquired during the L-H transition and the first two ELMs in shot 62744 is shown in figure 2(a). Group-delays from pulses with carriers inside 51-67GHz are shown. These were launched in O-mode polarization and are reflected when reaching densities between 3.2 and $5.6 \times 10^{19} \, \mathrm{m}^{-3}$. The pulse repetition rate was 8.33 MHz, permitting a scan through all frequencies in 1.68 μs.

Group-delay data from the L-mode section between 0.66 and 0.68 seconds features several characteristics different from the H-mode phase after $\sim$0.68 s. First, the group-delay differences between frequencies in L-mode are larger since the profile gradient is less steep than in H-mode (see gradients in the profiles in figure 2(c)). Second, the standard deviation of the reflected pulses is larger during L than H-mode at $\sim$100 ps versus $\sim$20 ps. Figure 2(b) shows the SPR raw data immediately before and after the ELM event. In figure 2(b) group-delays have been arbitrarily separated by 100 ps in order to allow better visibility of how individual group-delays change over time. Figure 2(c) shows the results of inverting group-delays from figure 2(a) into a density profile. Raw group-delays are averaged over 8.75 μs to produce each profile, which averages about 5 pulses in each frequency. It agrees within error bars with TS in both L and H-mode phases. The sources of uncertainty shown in the bottom of figure 2(c) include the limited beam size, reflection layer (Airy) width, TS magnitude errors, and TS mapping errors due to the magnetic reconstruction uncertainties [16].

The TS profile at 0.684 s (red profile in figure 2(c)) features a slightly hollow profile at $\rho_\psi \sim$0.9 which is not reproduced by SPR. Assuming density to be a flux function, this illustrates the drawback that a reflectometer launching from the low-field-side in O-mode polarization cannot distinguish between linear and hollow profiles since increasing frequencies sample exclusively high densities. Direct sampling may show evidence of wave tunneling, but an analog timing system sampling pulse group-delay exclusively cannot distinguish hollow profiles. Nonetheless, it must be noted that the TS profile shown is a fast snapshot which does not average over density fluctuations; average, steady-state, hollow profiles are not expected in the pedestal of H-modes.

Furthermore, it should be noted that data immediately at the ELM crash - a period of 0.5-0.7 ms when the D_α peak is observed in figure 2(a) - should be interpreted with caution. Group-delay data is interrupted by increased fluctuations at the ELM crash starting at 0.741 s: group-delay values appear quite scattered during this time. The analog pulse-timing system only records pulse group-delay and does not record any information on pulse width or
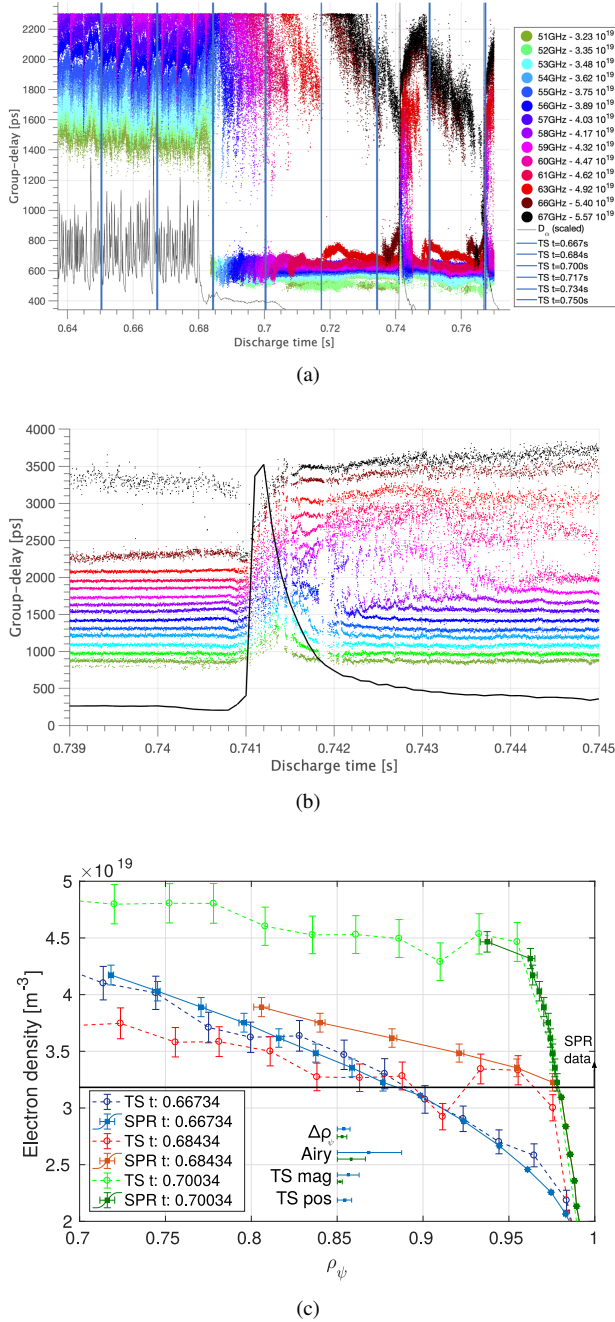
(a)

(b)

(c)

Figure 2. (a) SPR raw data in O-mode polarization across the L-H transition and the first two type-III ELMs in shot 62744. Frequencies 51-61GHz are being reflected from $\rho_\psi = 0.97$-0.955 with $k_\perp < 15\,\text{m}^{-1}$. Pulse return rates are ∼95%; (b) Zoom-in of raw-group delay data in (a) across the first ELM event. An arbitrary spacing of 100ps has been introduced between frequencies to improve visibility; (c) Sample density profile inversions compared with TS at three instances during the L-H transition.

amplitude. It cannot be ruled out that significant pulse dispersion occurs at these highly turbulent instances. In such cases, the reflected pulse group-delay is not well defined.

The conditional averaging (or conditional expecta-

tion [41]) procedure leading to mean inter-ELM density profiles is explained below. A peak in the D_α (656.3 nm filter) photodiode signal is used to identify the occurrence of an ELM: it provides the conditional probability for the ELM occurrence around which SPR data is averaged. The D_α signal responds to photons emitted by collisional excitation of neutral deuterium atoms in the divertor region which are excited by the energetic particles expelled by the ELM. A discharge with an almost steady ELM frequency is chosen and a period containing a large number of ELMs is taken for the conditional average. The first step is to obtain sound SPR group-delay data. Individual group-delays from a number of frequency sweeps (5-30 sweeps) are averaged to arrive at an unambiguous group-delay over frequency curve. This is required since, as seen in figure 2(b), there are instances where conditions at the cutoff layer can lead to 'missing' pulses. This occurs when the reflected pulse power is too low and the analog timing circuit cannot trigger into the reflected pulse power. Low reflected powers can occur in reflectometry due to scattering from the 2D nature of fluctuations at the reflection layer. Conway [42] showed that power variations between -2dB and -45dB can occur depending on the average size of the poloidal fluctuation correlation lengths and their radial amplitudes. During the peak of the D_α signal, pulse return rates are significantly affected; this provides a direct indication of the increased stochasticity of the cutoff layer at the ELM onset.

The second step proceeds to invert the group-delay curves over frequency into distances to the cutoff over frequency using the Abel inversion equation 1 shown above. The initialization $\partial\phi/\partial\omega$ (PG) curve in equation 1 above uses TS density profiles available at a 16 ms repetition rate. Hence, the group-delay curve under $f_0 = 50\,\text{GHz}$ is static in between TS sampling times. TS profiles measured 1 ms before and after the D_α peak are ignored because these can feature vastly different profiles that can result in erratic initialization curves. After applying the Abel inversion formula 1, the inverted distance-frequency information is then transformed into a density profile over ρ_ψ using the LIUQE magnetic reconstruction. The third and last step is to average the instantaneous density profiles obtained to get a mean inter-ELM profile. This is done by taking the D_α peak as the ELM indicator to find a mean ELM frequency. Profile SPR data is then split into ELMs based on the mean inter-ELM period. The average of these profiles is presented and discussed in section 5 below.

4. Plasma scenario overview

This section briefly presents an overview of the ELMy H-mode scenarios studied with SPR in this publication. Three different scenarios have been chosen to compare and contrast different types of ELMs. All scenarios feature lower single-null (LSN) diverted plasmas with a $B \times \nabla B$ drift in the favourable configuration towards the X-point.
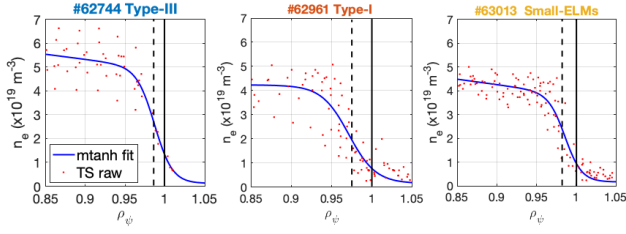
Figure 3. Pedestal density profile composite plot. In red are shown TS density raw data inside 75-90% of the ELM cycle period. In blue are shown profile fits using a 5-parameter modified hyperbolic tangent function [43][8]. Fit parameters are shown in table 1. Separatrix and pedestal locations are shown with black solid and black dotted lines, respectively.
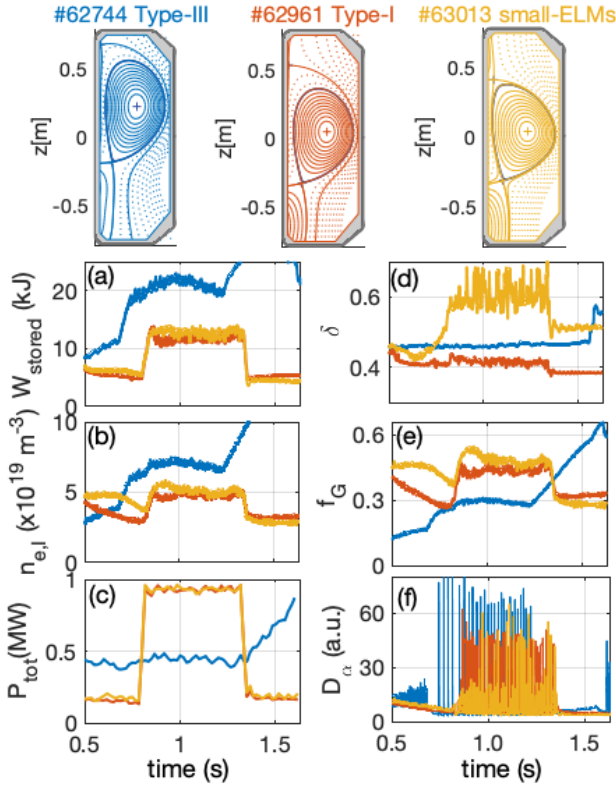

Figure 4. Comparison of plasma shape and time-traces of selected discharge parameters from the three ELM scenarios analyzed in this publication. (a) W_{stored} is the total stored energy calculated from integrating the pressure profile from the LIUQE magnetic reconstruction; (b) $n_{e,l}$ is the average plasma density measured with a vertical interferometer channel that travels across the plasma core; (c) P_{tot} is the total input power to the plasma both from internal ohmic heating and external neutral-beam heating; (d) δ refers to the edge plasma triangularity; (e) $f_G = n_{e,av}/n_G$ is the ratio between the volume averaged density and the Greenwald density limit (see [45]); (f) D_α is a vertical photodiode signal filtering 656.3nm radiation.

Table 1 presents common discharge parameters. Pedestal collisionality is defined as $\nu_{e,ped} \approx 0.1 Z_{eff} R_o n_{e,ped} T_{e,ped}^{-2}$ where pedestal values come from modified hyperbolic tangent [43] fits of TS profiles seen in figure 3.

Table 1 and figure 4 compare and contrast the three

different scenarios presented in this publication. The first scenario is an ohmic ELMy H-mode, first addressed in Weisen et al. [19]. It is a highly-reproducible H-mode scenario in TCV where 0.4 MW of ohmic power from a plasma current of 365 kA is sufficient to enter and maintain an ELMy H-mode. Its proximity to the upper lateral launcher antenna shown in figure 1 makes it ideally suited to study with the SPR diagnostic. The discharge studied features large average density and a relatively low pedestal collisionality. Each ELM releases about 8% of the stored energy. It is believed that this scenario features type-III ELMs because upon increasing the input power the plasma transitions into an ELM-free H-mode [20]. This type of ohmic H-mode ELMs have been termed 'large ELMs' [19] because of their relatively large energy losses at low pedestal collisitionality. Pitzchke [46][ch. 6] has found that the pressure gradient of this scenario is ideally MHD unstable, mainly limited by large-n numbers.

The second and third scenarios feature type-I and small ELMs, respectively. These are achieved by applying 1 MW of external heating by neutral-beam injection (NBI) at a relatively low plasma current of 168 kA. These two scenarios have been studied in a recent publication by Labit et al. [8]. In these plasmas a transition from type-I ELM to the small ELM scenario is possible if and only if the separatrix density is large enough, $n_{e,sep}/n_G \sim 0.3$, and the plasma triangularity is large enough, $\delta \geq 0.4$, (see figure 4). $n_G = I_P/(\pi a^2)$ refers to the Greenwald density limit, where n_G is the line-average density in units of $10^{20} m^{-3}$, I_P is the toroidal plasma current in mega Amperes, and a is the minor radius in meters [45]. As can be seen in table 1, the small ELM scenario features similar stored energy and normalized beta while releasing much less energy per ELM than its type-I ELM counterpart. Heat loads on the divertor target plates have been shown to decrease by a factor of six [8]. This relatively new TCV small ELM scenario has not been throughly experimentally characterized nor understood yet. Nevertheless, it is speculated that the ballooning transport is increased at the bottom of the pedestal because of the reduced shear (see [8] and [47]). Energy release per ELM is computed from the plasma stored energy derived from diamagnetic loop measurements, see Moret et al. [48] for details. The difference between plasma stored energy before and after the ELM is found and the average between ELMs during the steady-state ELMy phase of each shot is shown in table 1.

Note that the type-III ELM scenario studied here features higher energy confinement time and stored energy than the type-I and small-ELM scenarios. This is particular to the scenarios chosen for this study. The improved confinement in 62744 is due to its larger plasma current and lower amount of external heating power, in agreement with the energy confinement $\tau_{e-IPB98(y,2)}$ scaling featuring $I_P^{0.94}$ and $P^{-0.68}$ terms. The following section 5 presents average

ELM type	III	I	Small	stdev
Discharge number	62744	62961	63013	$\pm$
Plasma current, I_P (kA)	365	168	168	5
Total heating power (MW)	0.5	0.83	0.84	0.1
Total radiated power (MW)	0.17	0.17	0.18	0.01
Safety factor at $\rho_\psi = 0.95$, q_{95}	2.4	4.6	4.9	0.2
Line average $n_{e,l}$ [10^{19} m^{-3}]	5.9	3.9	4.2	0.2
Elongation κ	1.70	1.54	1.53	0.05
Triangularity δ	0.46	0.41	0.59	0.03
Top triangularity δ_u	0.25	0.20	0.61	0.08
Normalized beta $\beta_N = \beta \frac{aB_T}{I_P}$ [%]	1.15	1.54	1.67	0.07
Energy stored W_{MHD} [kJ]	21.2	11.8	12.9	0.8
Effective charge, Z_{eff} (ρ_ψ =0.9-1.0)	1.5	1.2	1.3	0.2
Fractional energy loss per ELM, $\frac{\Delta W_{ELM}}{W_{tot}}$ (%)	8	12	5	1
Energy confinement time [ms]	54	26	25	$\sim$10%
Energy confinement enhancement factor $H_{IPB98(y,2)}$ [44]	0.96	1.04	1.19	$\sim$10%
Mean ELM frequency [Hz]	61 $\pm$ 14	124 $\pm$ 29	166 $\pm$ 32	
Pedestal density $n_{e,ped}$ [10^{19} m^{-3}]	4.9$\pm$ 0.6	4.2 $\pm$ 0.6	3.91 $\pm$ 0.2	
Separatrix density $n_{e,sep}$ [10^{19} m^{-3}]	1.3	0.76	0.954	$\sim$10%
Pedestal width $\Delta\rho_{\psi,ped}$	0.011$\pm$0.009	0.017$\pm$0.006	0.011$\pm$0.003	
Pedestal location $\rho_{\psi,n_{e,ped}}$	0.987$\pm$0.015	0.982$\pm$0.008	0.987$\pm$0.003	
Pedestal collisionality, $\nu^*_{e,ped}$	1.1$\pm$0.3	1.12$\pm$0.4	1.13 $\pm$0.4	

Table 1. Discharge parameters of ELM scenarios analyzed in this publication. Values shown are averages $\pm$ standard-deviations inside the quasi-steady-state ELMy H-mode phase. The stdev column corresponds to the largest standard deviation of all three shots in order to give a maximum error estimate.

inter-ELM density profile evolution in these three regimes.

5. Inter-ELM density profiles

5.1. Type-III

Figure 2(a) shows the SPR raw data through the L-H transition and the first two ELMs of shot 62744. Using the Thomson scattering (TS) density profile at 0.75 s, output frequencies from 51 to 61 GHz are estimated to cover the range $\rho_\psi = 0.967$-0.955 with $k_\perp < 35$ m^{-1}. Frequencies 63, 66, and 67 GHz are also included to observe deeper cutoff layers at $\rho_\psi = 0.952$, 0.9372, 0.88 albeit with poorer alignment ($k_\perp = 18$, 35, and 88 m^{-1}, respectively). During the H-mode phase under study, pulse return rates for frequencies 51-61 GHz are above 95% while for 63-67 GHz they are about 75% in average. Figure 2(a) includes a scaled D_α signal which shows a clear dip about 1.3 ms before the ELM crash. Simultaneously, SPR data shows a marked change in group-delay at all frequencies $\sim$1.3 ms before the ELM event. Figure 2(b) shows a close-up of the SPR raw data across the first ELM. The latter figure shows frequency 67 GHz in black reflecting beyond the pedestal for most of the inter-ELM period and joining the pedestal just before the onset of the ELM. This observation is consistent with a large density gradient leading to an ELM crash. Type-III ELM D_α and SPR precursor signals are not unique to TCV. Type-III ELMs are known to feature clear magnetic precursor oscillations with toroidal mode number n$\approx$5-10 and poloidal mode number m$\approx$10-15 in other machines [5] [14] [7].

As described in section 3 above, peaks in the D_α signal are used to time ELMs and perform conditional averaging. 23 ELMs with a frequency $f_{ELM} \sim$ 63 Hz$\pm$14 have been considered between 0.8325 and 1.223 s during discharge 62744. Prior to inverting the group-delay information into profiles, figure 5 shows conditional averaging performed in the raw-data in order to observe the average group-delay data behaviour. Error bars of average group-delays correspond to the standard deviation of the group-delays in each synchronized ELM event divided by the square root of the number of ELM events taken in the average. These errors stay between 2-10 ps for frequencies that remain in the pedestal and can reach 80-100 ps for frequencies that remain in the L-mode-like region beyond the pedestal. Such low pedestal group-delay standard deviation would correspond to a range-precision of <1.5 mm in vacuum. This provides confidence that the diagnostic can sample average pedestal behaviour with a group-delay precision *exceeding* that of a static mirror with 10dB power variations at 17 ps. Frequencies 66 and 67 GHz, which reflect mostly beyond the pedestal, show that the density profile is not
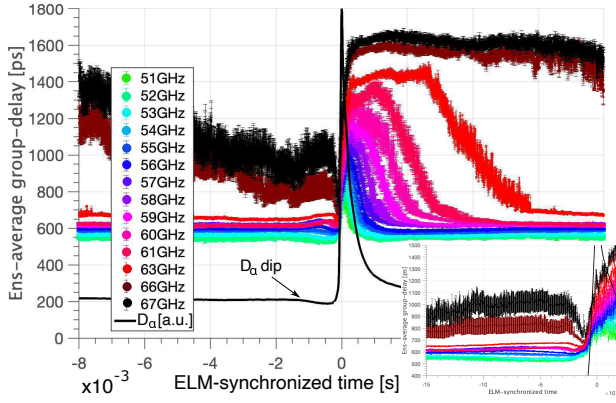
Figure 5. Conditional mean inter-ELM SPR group-delay data from 23 ELM events inside 0.83-1.4 s during discharge 62744.

Figure 6. Conditional mean SPR density profile (pedestal top, O-mode) obtained from 23 type-III ELM events inside 0.83-1.4 s during discharge 62744.

Figure 7. Local density gradient ($\Delta n_e / \Delta \rho_\psi$) evolution ∼1.3 ms before ELM onset from profiles in figure 6. Average values of ρ_ψ 2 ms before the ELM have been taken to localize the average cutoff of each frequency.

static. The continuous decrease in group-delay is indicative of an increasing gradient in the density profile beyond the pedestal. Figure 5 also shows that the slight decrease in the D_α signal ∼1.3 ms before the ELM is accompanied by marked changes to the conditionally averaged group-delays.

Prior to inverting profiles, the group-delays from 5 consecutive sweeps are averaged in order to reduce the impact of unrecorded pulses. Since there are 14 frequencies in every sweep at a pulse repetition rate of 1/8.33 MHz = 0.12 μs, a single sweep is achieved in 1.68 μs. The chosen 5-sweep averaging leads to an effective profile resolution of 8.4 μs. The Abel inversion algorithm is then used to invert group-delay data as described in section 3 above. Only frequencies 51-61 GHz could be taken into account because the algorithm needs equally-spaced frequency steps. The inversion results can be seen in figure 6. The latter figure includes a 'TS-reference'. It indicates the average ρ_ψ position of the last initialization group-delay obtained from TS density profiles and the LIUQE magnetic reconstruction. It does not evolve through the ELM event since the ELM is a highly turbulent phenomenon and features a high amplitude of magnetic field fluctuations [5]. The magnetic reconstruction cannot be fully trusted in the presence of these large fluctuations. Thus, the initialization uses values 1ms before and after the ELM and keeps them constant across the ELM crash, as outlined in section 3.

Figure 6 shows a number of interesting features. Firstly, as remarked above, a distinct evolution of the profile ∼1.3 ms before the ELM event can be clearly observed. In order to further characterize this precursor behaviour, the 'local' profile gradients ($\Delta n_e / \Delta \rho_\psi$) between adjacent frequencies are plotted in figure 7.

Figure 7 shows that the local profile gradients appear to pivot around a constant gradient at $\rho_\psi = 0.97$ as the D_α signal dips at ∼1.3 ms. The local gradient outside $\rho_\psi > 0.971$ becomes steeper following the dip. The local gradient inside $\rho_\psi < 0.97$ shows, initially, a time-dependent gradient
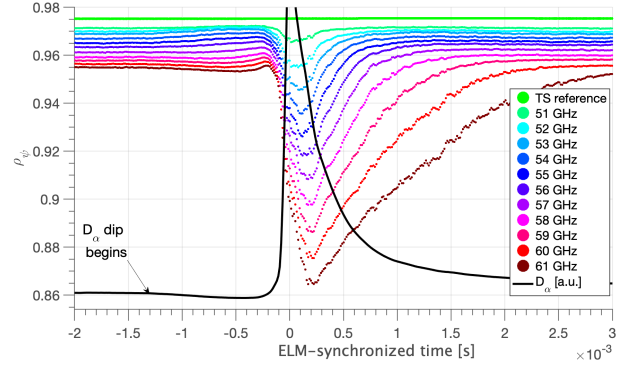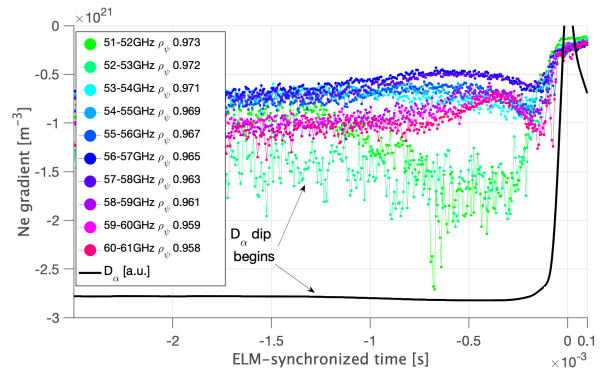
relaxation which begins with frequencies 56-58GHz at $\rho_\psi = 0.967$-0.963. This relaxation then proceeds through regions further inside the pedestal: $\rho_\psi = 0.961$-0.958. The decrease in gradient is more pronounced - by roughly a factor of two compared with $\rho_\psi = 0.967$-0.963 in the regions deeper inside. About 350 μs before the ELM, the local gradients inside $\rho_\psi < 0.97$ begin to reverse their relaxation and grow steeper. Just as these gradients return to their values prior to the D_α dip, local gradients outside $\rho_\psi > 0.97$ begin to reverse their initial steepening. When local gradients return to their pre-D_α-dip values, the local gradients outside $\rho_\psi > 0.97$ begin a sharp relaxation which is accompanied by a growth of the D_α signal.

In short, the average profile of this ohmic type-III ELM scenario shows a clear precursor ∼1.3 ms before the ELM-crash. The density profile outside and inside $\rho_\psi = 0.97$ behave quite differently during this precursor. The fact that the gradient of the density profile outside ρ_ψ 0.97 grows larger before the ELM crash is consistent with the MHD-stability picture of the ELM crash being triggered by the gradient exceeding a maximum threshold. Pitzschke et al. [20] also reported an increase in the gradient of TS density profile fits prior to the onset of type-III ELMs. The

gradient growth reported by Pitzschke [20] starts occuring ∼2 ms before the ELM crash. Nunes et al. [49] identified a similar pivot-point for type-I ELMs in AUG also at about $\rho_\psi \sim 0.97$ but during the recovery phase of the ELM cycle. Nunes et al. [49] report that the profile outside the pivot point recovers at a constant rate regardless of plasma conditions, while the profile inside the pivot point recovers at a rate dependent on the ELM frequency.

Another evident feature of figure 7 is that the collapse of the gradients precede the peak in the D_α signal. Local gradients at $\rho_\psi = 0.973$ begin to relax first at about ∼0.3ms before the D_α peak. The entire pedestal reaches a common small gradient before the D_α fully peaks. It is worth noting that precisely when the local gradients at $\rho_\psi = 0.973$ start decreasing, the D_α signal starts slowly increasing. Furthermore, it is interesting to note that the outer local gradients relax first. Thus the ELM crash appears to occur in the steep gradient region and build towards the pedestal top and the core.

5.2. Type-I

Figure 8 shows the raw SPR and D_α data during the L-H transition and the first few large ELM events during discharge 62961, featuring type-I ELMs. While the large type-I ELMs are clearly defined, there are many smaller pedestal relaxations seen in both the D_α and SPR. These events are ignored by the conditional averaging procedure but lead to a less smooth mean D_α and SPR profile as seen in figure 9. Pulse return rates are in the order of 40-50%. The magnetic axis is located at the vertical vertical position z=0 cm, which corresponds to the middle of the vessel (see equilibria for 62961 in figure 4). There is, therefore, a larger distance between the launcher antenna and the plasma cutoff. This larger distance leads to an increase in the sampling beam radius and hence a decrease in the amount of beam power density reflected back into the receiving antenna.

Plasmas at z=0 cm hence feature a poorer signal to noise ratio and more missed pulses. Fortunately, temporal resolution can be sacrificed to still access unambiguous profile information. Figure 9 shows the conditionally averaged inter-ELM profile from 56 ELMs ($f_{ELM} \sim$124 Hz) between 0.858 and 1.34 s during discharge 62961. 20 frequency sweeps (at 7 frequencies per sweep) have been used to ensure all time points contain meaningul group-delays for all frequencies, resulting in a profile time resolution of 16.8 μs.

Important observations can be made from figure 9. Although the SPR data cannot be fully trusted at the ELM crash given the increased amount of power scattering, the spatio-temporal evolution of group-delays during the ELM recovery phase can be considered to be an accurate reconstruction. Figure 8 shows a strong interruption of group-delay data at the ELM event but a consistent recovery phase for frequencies 51-56 GHz.
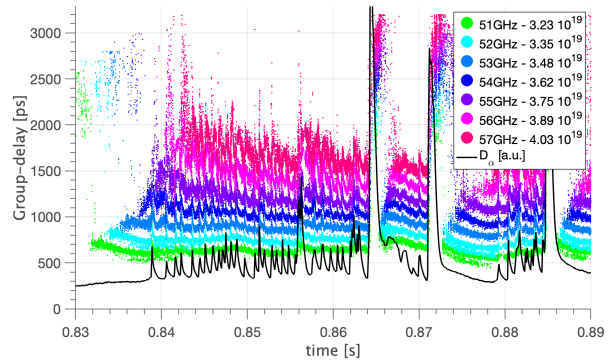

Figure 8. SPR data in O-mode polarization during the first few ELMs in shot 62961. Frequencies 51-57 GHz are being reflected from $\rho_\psi =$ 0.955-0.97 with $k_\perp <$15 m^{-1}. Pulse return rates are above 40% in all frequencies. Group-delays have been artificially separated by 100 ps to improve the visibility of individual frequencies.

One evident feature of the raw data shown in figure 8 is that the inter-ELM relaxation events appear to strongly perturb the group-delays of pulses from high frequencies such as 56 and 57 GHz more than 51 and 52 GHz. The average profile inversion in figures 9 and 10 reveals that the relaxations affect more strongly the pedestal inside $\rho_\psi \lesssim$ 0.965 than outside. While the perturbation is not fully localized, it can be proposed that these small inter-ELM relaxations do not affect strongly the steep-gradient region.

There are marked temporal and spatial evolution differences between type-III and type-I scenarios. Firstly, the average D_α signal shows a less well-defined peak over time. In the case of type-III ELMs (figure 6), the average D_α reaches its peak in 0.1 ms whereas the average D_α in figure 9 takes 0.5 ms. Also, the SPR density profile in figure 9 seems to recover more slowly than the type-III ELM profile in figure 6. Namely, frequency 56 GHz takes over 3 ms to rejoin the pedestal in type-I ELMs versus just about 1ms in the type-III ELMs. The faster recovery of the type-III ELM scenario can be explained in the basis of its larger energy confinement time (see table 1).

There are also spatial differences between both scenarios. Figure 9 shows that frequency 56 GHz starts growing back into the pedestal from $\rho_\psi = 0.85$. In contrast, in figure 6, during a type-III ELM, frequency 56 GHz recovers back into the pedestal from $\rho_\psi = 0.92$. These observations show, as expected [5] [7], that type-I ELMs affect a larger plasma volume (and thus result in a larger release of plasma energy) than type-III. The density profile seems, unequivocally, to recover more slowly and from deeper in the core after a type-I ELM. Nunes et al. [49] have reported type-I ELMs can affect up to 20-40% of the plasma minor radius, which is consistent with the observations above.

Figure 10 shows the local gradients prior to the ELM crash. It shows that in the type-I ELM scenario studied here, there is no clear precursor in either the D_α or SPR data. This
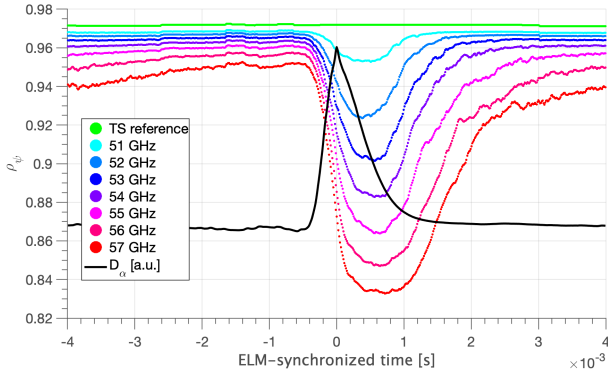
Figure 9. Ensemble average SPR density profile (pedestal top, O-mode) obtained from 55 type-I ELMs in the interval 0.8583-1.34 s during discharge 62961.

Figure 10. Local density gradient evolution ∼1ms before ELM onset from profiles in figure 9. Average values of ρ_ψ 2 ms before the ELM have been taken to localize the average cutoff of each frequency.

can be due to the lack of a measurable precursor within the chosen temporal averaging of SPR data at 16.8 μs. Leonard et al. [6] indicate that the ELM instability grows in a few tenths of Alfven times ∼10 μs, thus it is likely that at the averaging chosen, the precursor is obscured. However, the precursor could also be hidden by the conditional averaging procedure performed in the presence of the inter-ELM pedestal relaxations seen in figure 8. Lastly, it could be that the precursor is found in a portion of the pedestal not sampled in the present study.

Figure 10 shows that the gradient is lower in layers deeper inside the plasma, indicating that the reflectometer is sampling the top portion of the pedestal, on average. Prior to the ELM crash, it can be observed in the gradients of figure 10 that the cutoff layer at ρ_ψ =0.968 relaxes prior to that at ρ_ψ =0.955. This suggests that the profile gradient relaxation that leads to the ELM crash and the D_α peak begins in the outer portions of the pedestal and builds into the core. This is similar to what is observed in figure 7. Another similarity with figure 7 is that the D_α signal begins slowly increasing only once the local gradients of the lowest frequency pair (ρ_ψ =0.968) begin to relax. Thus, the pedestal gradient collapse precedes also the D_α peak.

5.3. Small ELMs

Figure 11 shows the raw SPR and D_α data through the L-H transition and first few ELM events of discharge 63013 featuring "small ELMs". There are no inter-ELM perturbations as in 62961; however, the D_α peak is no longer as well defined as in the two scenarios above. Pulse return rates for this discharge are about 20-54% in average; the vertical location of the magnetic axis is also z=0 cm as in 62961.

Figure 12 shows the conditionally averaged inter-ELM profile. This average profile comes from 26 ELMs (f_{ELM} ∼137 Hz) between 0.834 and 1.046 s. 40 frequency sweeps (at 10 frequencies per sweep) have been taken to calculate a single group-delay in order to ensure all time
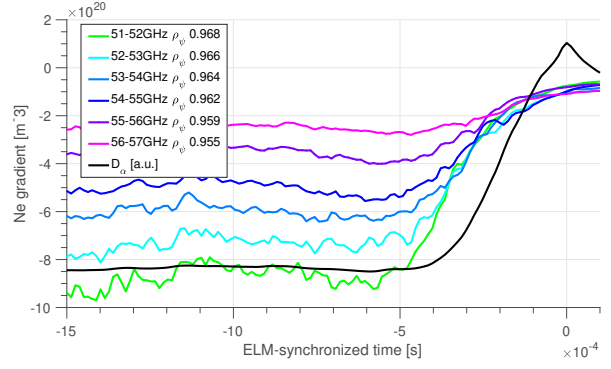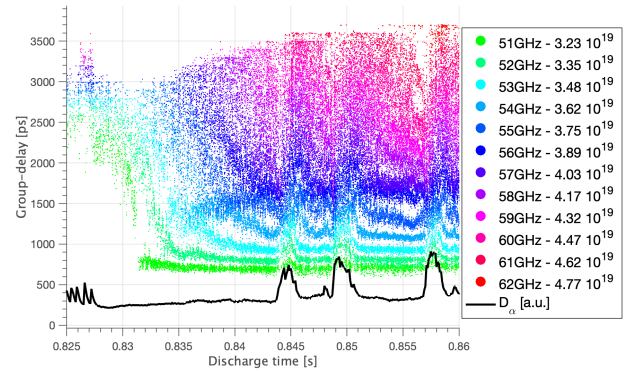

Figure 11. SPR data in O-mode polarization during the first few ELMs in shot 63013. Frequencies 51-60 GHz are being reflected from ρ_ψ =0.93-0.98 with $k_\perp$ <15 m^{-1}. Pulse return rates are about 32-54% at all frequencies.

points contain meaningful group-delays for all frequencies, resulting in an average profile time resolution of 48 μs. Frequencies 61 and 62 GHz have been discarded from the profile analysis because they feature low pulse return rates and appeared only before the small-ELM crash.
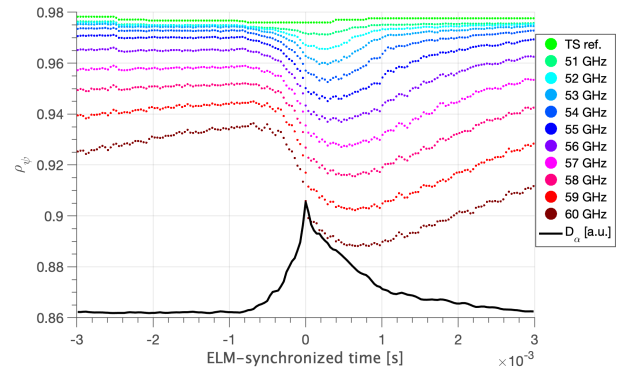

Figure 12. Ensemble average SPR density profile (pedestal top, O-mode) obtained from 26 small ELMs inside 0.834-1.05 s during discharge 63013.

Figure 12 shows unique features of the small-ELM

density pedestal top. Firstly, the pedestal does not seem to fully recover in the sample density space sampled (51-60 GHz). While in figures 6 and 9 the density profile seems to recover its pedestal shape in roughly about 2-3 ms, figure 12 shows that the density profile of the small-ELM scenario is constantly evolving. Cutoff layers recover more slowly and do not really form a steep pedestal until the next small ELM arrives.

Another evident feature is that the ELM event does not penetrate very far into plasma. Namely, frequency 56 GHz penetrates up to ρ_ψ =0.935 in the small-ELM 63013 whereas in the type-I ELM case above, it penetrates up to ρ_ψ =0.85. This difference is larger than what could be accounted for based solely on the differences in density between both discharges. The type-I ELM scenario does feature a pedestal density of 4.2±0.6 m^{-3}, slightly larger than the small-ELM scenario at 3.9± 0.2 m^{-3} (see table 1). One millisecond prior to the ELM, frequency 56 GHz reflects from ρ_ψ =0.955 and ρ_ψ =0.965 during the type-I and small-ELM scenarios, respectively. Thus the slight difference in density between both shots accounts for a difference in ρ_ψ of only 0.01. Therefore, the large change in ELM penetration from ρ_ψ = 0.85 to 0.935 between type-I and small-ELMs does indicate a stronger perturbation of the density profile in the type-I ELM scenario. A stronger density perturbation is expected in the type-I ELM scenario also because the small-ELMs release 5% of the stored energy per ELM (see table 1) versus 12% in the type-I ELM scenario.

However, it must be noted that as presented in section 3, during the ELM crash event pulse dispersion can occur and group-delays cannot be trusted from the analog timing circuits. Also, profile initialization ignores TS profiles and equilibrium reconstructions 1 ms before and after the ELM, thus the group-delay curve under 50 GHz remains static through the highly dynamic ELM crash. Improved analysis methods using dynamic initialization and direct pulse sampling approaches should be implemented if robust quantitative results regarding the amount of ELM penetration are to be inferred.

Figure 13 shows the evolution of the local gradients 1.5 ms prior to the small-ELM crash. No clear precursors are observed. Figure 13 shows that the reflectometer is looking at the transition between pedestal and main core plasma, as was the case in the type-I ELM scenario. Figure 13 shows that frequencies above 56 GHz reflecting deeper inside than ρ_ψ =0.962 feature a very small gradient which indicates that these are mostly beyond the pedestal top. At ρ_ψ = 0.97, figure 13 shows a more abrupt transition between pedestal and main plasma since the gradient between frequencies 56-57 GHz at ρ_ψ = 0.962 and 53-54 GHz at ρ_ψ = 0.974 differs by a factor of ×3 1 ms before the small-ELM event. During the type-I ELM, the same frequency interval leads to a difference of only about ×2.

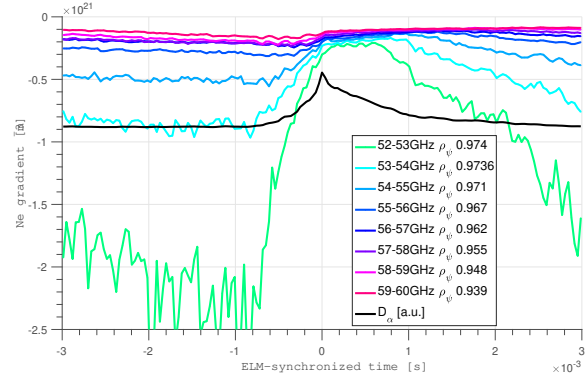**Figure 13.** Local density gradient evolution ∼1 ms before ELM onset from profiles in figure 12. Average values of ρ_ψ 1 ms before the ELM have been taken to localize the average cutoff of each frequency.

Figure 13 shows, alike figures 7 and 10, that the local gradient from the steep-gradient region ρ_ψ =0.974 relaxes well prior to the D$_\alpha$ peak. Also, the small-ELM crash begins in the steep gradient region and builds towards the core. However, in contrast with figures 7 and 10, the gradients in figure 13 do not reach a common minimum prior to the D$_\alpha$ peak and appear to continuously evolve.

6. Inter-ELM density fluctuations

Studying the power spectral density (PSD) of SPR group-delays has revealed the potential to identify macroscopic density fluctuations. SPR has been able to identify sawtooth oscillations in agreement with interferometry diagnostics as well as ELM-free H-mode quasi-coherent modes in agreement with magnetic pick-up coil diagnostics [16]. Although the quantitative interpretation of group-delay oscillations as density fluctuations requires theoretical modeling that is still missing, signatures of macroscopic oscillations with k$_\perp$ <2.6 cm^{-1} (beam radius ∼1.5 cm [18]) can be observed in SPR's PSDs.

Figure 14 illustrates the finding of a quasi-coherent oscillation at the bottom of the small-ELM scenario pedestal presented above in section 5.3. An identical discharge to 63013, 63003 was used to sample the bottom of the pedestal with the X-mode polarization, which samples lower densities as shown in figure 14(a). Figure 14(b) shows the spectrogram of frequency 58 GHz which is reflected near the separatrix. Figure 14(c) shows a snap of this spectrogram at t =0.8914s, and it shows a clear peak at ∼32 kHz. Pulse return rates are 67%. Linear interpolation is used to approximate the group-delay of missing pulses. Pulses with a carrier frequency of 69 GHz were also measured during this discharge (ρ_ψ ∼0.988-0.993) but the oscillation was not clearly identified. Figure 14(e) shows the power spectral density function of the *same* 58 GHz frequency during an identical shot, 63013, using O-mode polarization looking at ρ_ψm0.95 where the mode cannot

(a)
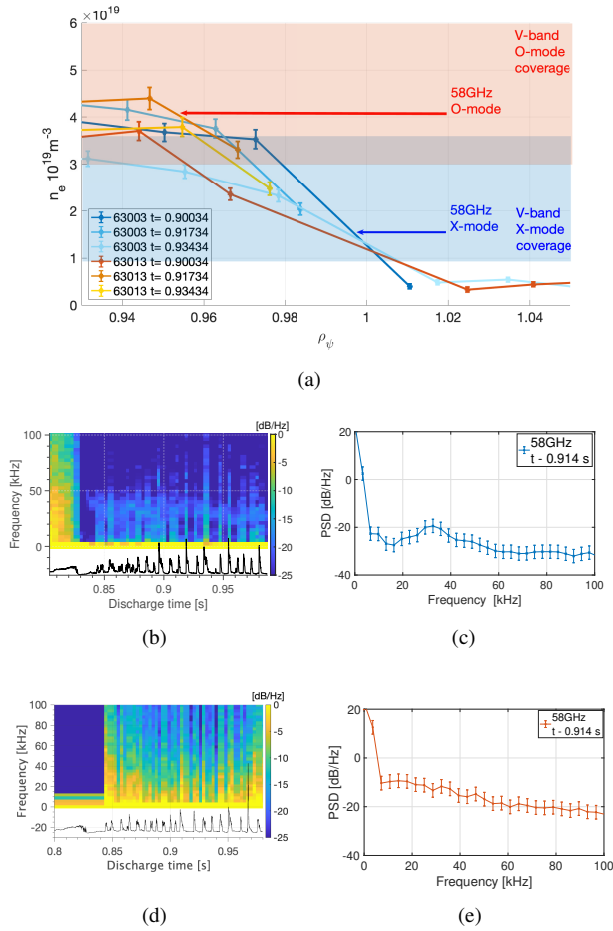

(b)

(c)

(d)

(e)

Figure 14. Comparing group-delay fluctuations during small-ELM scenario using different reflectometer polarizations. (a) Average localization of O/X-mode coverage in discharge 63013(O-mode) and repeat 63003 (X-mode). Raw TS profiles are shown for three times surrounding t=0.914 s for both shots. (b) Spectrogram of inter-ELM oscillations in X-mode polarization during discharge 63003. 4 ms windows, f=58 GHz, ρ_ψ ~1.0; (c) PSD of spectrogram in 14(b) at t=0.914 s; (d) Spectrogram of inter-ELM oscillations in O-mode polarization during discharge 63013. 4 ms windows, f=58 GHz, ρ_ψ ~0.95; (e) PSD of spectrogram in 14(d) at t=0.914 s.

be observed. The mode cannot be observed in any of the frequencies in O-mode down to 51 GHz (ρ_ψ ~0.97) ruling out that the mode is found in the pedestal top.

Spectral analysis of SPR data during type-I ELM discharges in either X or O-mode polarization have failed to reveal any such clear oscillation. Section 5.2 showed profile data from discharge 62961 in O-mode polarization. These discharge was repeated and sampled using X-mode polarization in 62997. However, spectral analysis of group-delay data from either discharge failed to reveal any clear oscillation. Considering that both type I and small-ELM scenarios have similar plasma properties except for triangularity, it can be ascertained that the ~32 kHz oscillation appears in the *bottom* (ρ_ψ =0.993-1.05) of the small-ELM H-mode pedestal exclusively.

Figure 15 shows the results of spectral analysis of
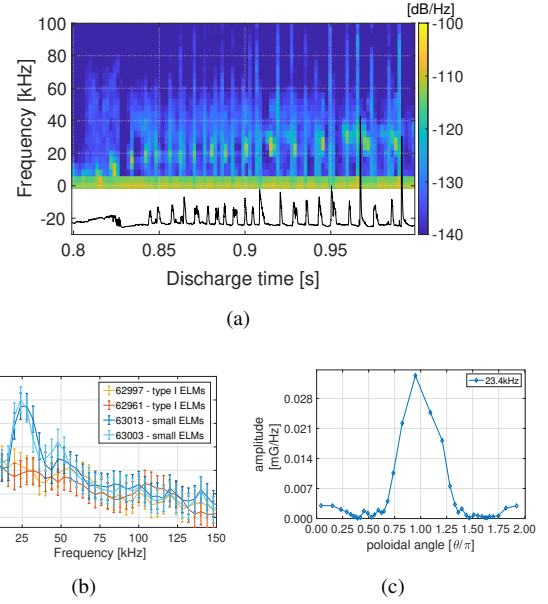

(a)

(b)

(c)

Figure 15. Comparing group-delay fluctuations during small-ELM scenario using different reflectometer polarizations. (a) Spectrogram of magnetic pick up coil number 20 in poloidal array in sector 3, located in the low-field side equator during small ELM 63013/63003. D_α signal is shown for reference in black. (b) Power spectral density of above-mentioned probe at 0.914 s (1 ms PSD window) during type-I ELM: 62961/62997 and small ELM 63013/63003 discharges showing the ~23 kHz mode in the small-ELM discharges exclusively. (c) Poloidal amplitude dependance of magnetic signals at 0.914s in 63013 filtered inside 20-25kHz using the poloidal array in TCV's sector 3.

magnetic pick up (Mirnov) coil diagnostics [40] during the H-mode scenarios presented here. It has been observed that a ~23kHz oscillation is observed exclusively during the small-ELM discharges. Figure 15(a) shows a spectrogram of a magnetic pick-up coil signal located in the low-field-side equator ($z = 0$ cm) during the small-ELM dishcarge 63013. It shows an intermittent mode growing in frequency through the first small-ELMs up to 25-30 kHz appearing in-between small ELMs. Figure 15(b) shows the power spectral density over frequency at 0.914 s inside a 1 ms window. A quasi-coherent mode peaked at roughly ~23 kHz is seen in rough agreement with the mode observed by SPR shown in figure 14(c). It must be noted that spectrograms in figure 14(b) for SPR and 15(a) for the magnetic coil do not show the same frequency evolution of the mode over time. SPR's mode maintains a steady frequency and does not seem intermittent, in contrast to the magnetic coil spectrogram.

Figure 15(b) shows that this mode is not observed during 62997 nor 62961 type-I ELM discharges, in agreement with SPR observations. Also, figures 14(c) and 15(b) show that the modes do not have the same frequency. SPR shows the mode to be at about ~32 kHz, while the magnetics observe a peak at ~23 kHz, instead. The difference in frequency can be due to the fact that SPR measures in a specific location, which, due to a particular

ExB rotation velocity, can result in a different Doppler shift. Magnetic field oscillations are measured near the vessel wall and are not local. It is also possible that both oscillations observed are not the same mode.

Toroidal mode number analysis of the $\sim$23 kHz oscillation reveals a strongly linear cross-phase characteristic of a n=+1 toroidal mode propagating counter-clockwise around the machine looking from the top (counter to the plasma current). Poloidal mode number analysis is complicated by the strongly negative plasma shape ($\delta =0.59$) and the limited number of magnetic probes along the highly-elongated TCV vessel [50]. Two preliminary observations can be made about the poloidal nature of the $\sim$23 kHz mode. First, it appears only in 2 probes above and below the low-field side mid-plane as seen in figure 15 (c). Hence, it appears to feature a ballooning character. Secondly, only a high m-number can be speculated from the limited amount of cross-phase measurements available.

The observation of a common oscillation in both SPR and magnetic coil data exclusively during the small-ELM discharges provides experimental evidence of an oscillation potentially partially responsible for the different pedestal dynamics of small versus type-I ELMs. More experiments are required to scan the pedestal throughly using the full band of frequencies in both polarizations in addition to further characterizing the dependencies of this mode on plasma conditions.

7. Conclusions

New pedestal top density measurements of three different ELMy H-mode scenarios in TCV have been presented with unprecedented spatio-temporal resolution using a short-pulse reflectometer (SPR). Conditionally-averaged inter-ELM profiles have been generated with temporal resolutions between 8 to 40 μs and radial resolutions of $\rho_\psi \sim 0.002$.

An ohmic H-mode discharge featuring type-III ELMs has been observed to show a very clear precursor about 1.3 ms before the characteristic D_α ELM spike. Local density profile gradients above and below $\rho_\psi = 0.97$ show contrasting behaviour throughout this 1 ms precursor period. A piecewise increase in the density pedestal gradients outside $\rho_\psi > 0.97$ is accompanied by an opposite gradient relaxation inside $\rho_\psi < 0.97$ prior a steady global pedestal relaxation leading to the D_α ELM spike. By contrast, type-I and small-ELM scenarios studied here do not show precursors in the region sampled. The lack of precursors during type-I and small-ELM scenarios down to the 10s of microsecond of group-delay averaging motivates the development of faster temporal resolution. This is potentially achievable using pulse interleaving with direct sampling SPR [16]. While more experiments are needed to cover a larger range of plasma conditions and densities using the X-mode polarization, these intriguing dynamics

can serve already as a solid experimental basis for non-linear MHD model validation.

It has also been observed consistently in all scenarios studied here that the local pedestal density gradient relaxes *before* the D_α signal peaks. This pre-ELM profile relaxation begins in the steep-gradient region ($\rho_\psi \sim 0.97$) and builds into the core. In both the type-III and type-I ELM scenarios, all local gradients relax and reach a minimum prior to the D_α peak, while in the small-ELM scenario the global gradient continues to relax beyond the maximum in D_α.

Lastly, a 25-35 kHz quasi-coherent mode has been identified with both the SPR and magnetic coil diagnostics during the small-ELM scenario in contrast to a very similar type-I ELM discharge. SPR allows to localize the mode in the pedestal bottom ($\rho_\psi \sim$0.993-1.05). Magnetic probe analysis shows a $n = +1$ toroidal mode number and a ballooning character. More experiments are required to thoroughly sample the entire pedestal region and study the mode dependencies. Nonetheless, the identification of this oscillation is an important step towards a better understanding of the effects of plasma shape and fueling in the transport dynamics of H-mode pedestals.

These initial results have proven the SPR diagnostic to be a powerful new tool to investigate the properties of the pedestal with unmatched spatial and temporal resolution.

8. Acknowledgments

References

[1] Shimada M, Campbell D, Mukhovatov V, Fujiwara M, Kirneva N, Lackner K, Nagami M, Pustovitov V, Uckan N, Wesley J, Asakura N, Costley A, Donné A, Doyle E, Fasoli A, Gormezano C, Gribov Y, Gruber O, Hender T, Houlberg W, Ide S, Kamada Y, Leonard A, Lipschultz B, Loarte A, Miyamoto K, Mukhovatov V, Osborne T, Polevoi A and Sips A 2007 *Nuclear Fusion* **47** S1–S17 ISSN 0029-5515, 1741-4326
[2] Wagner F, Becker G, Behringer K, Campbell D, Eberhagen A, Engelhardt W, Fussmann G, Gehre O, Gernhardt J, v Gierke G,

Haas G, Huang M, Karger F, Keilhacker M, Klüber O, Kornherr M, Lackner K, Lisitano G, Lister G G, Mayer H M, Meisel D, Müller E R, Murmann H, Niedermeyer H, Poschenrieder W, Rapp H, Röhr H, Schneider F, Siller G, Speth E, Stäbler A, Steuer K H, Venus G, Vollmer O and Yü Z 1982 *Physical Review Letters* **49** 1408–1412 ISSN 0031-9007

[3] Wagner F 2007 *Plasma Physics and Controlled Fusion* **49** B1–B33 ISSN 0741-3335, 1361-6587

[4] Moret J M 2005 *Review of Scientific Instruments* **76** 073507 ISSN 0034-6748, 1089-7623

[5] Zohm H 1996 *Plasma Physics and Controlled Fusion* **38** 105–128 ISSN 0741-3335, 1361-6587

[6] Leonard A W 2014 *Physics of Plasmas* **21** 090501 ISSN 1070-664X, 1089-7674

[7] Suttrop W 2000 *Plasma Physics and Controlled Fusion* **42** A1–A14 ISSN 0741-3335, 1361-6587

[8] Labit B, Eich T, Harrer G, Wolfrum E, Bernert M, Dunne M, Frassinetti L, Hennequin P, Maurizio R, Merle A, Meyer H, Saarelma S, Sheikh U, Adamek J, Agostini M, Aguiam D, Akers R, Albanese R, Albert C, Alessi E, Ambrosino R, Andrèbe Y, Angioni C, Apruzzese G, Aradi M, Arnichand H, Auriemma F, Avdeeva G, Ayllon-Guerola J, Bagnato F, Bandaru V, Barnes M, Barrera-Orte L, Bettini P, Bilato R, Biletskyi O, Bilkova P, Bin W, Blanchard P, Blanken T, Bobkov V, Bock A, Boeyaert D, Bogar K, Bogar O, Bohm P, Bolzonella T, Bombarda F, Boncagni L, Bouquey F, Bowman C, Brezinsek S, Brida D, Brunetti D, Bucalossi J, Buchanan J, Buermans J, Bufferand H, Buller S, Buratti P, Burckhart A, Calabrò G, Calacci L, Camenen Y, Cannas B, Cano Megías P, Carnevale D, Carpanese F, Carr M, Carralero D, Carraro L, Casolari A, Cathey A, Causa F, Cavedon M, Cecconello M, Ceccuzzi S, Cerovsky J, Chapman S, Chmielewski P, Choi D, Cianfarani C, Ciraolo G, Coda S, Coelho R, Colas L, Colette D, Cordaro L, Cordella F, Costea S, Coster D, Cruz Zabala D, Cseh G, Czarnecka A, Cziegler I, D'Arcangelo O, Dal Molin A, David P, De Carolis G, De Oliveira H, Decker J, Dejarnac R, Delogu R, den Harder N, Dimitrova M, Dolizy F, Domínguez-Palacios Durán J, Douai D, Drenik A, Dreval M, Dudson B, Dunai D, Duval B, Dux R, Elmore S, Embréus O, Erdõs B, Fable E, Faitsch M, Fanni A, Farnik M, Faust I, Faustin J, Fedorczak N, Felici F, Feng S, Feng X, Ferreira J, Ferrò G, Février O, Ficker O, Figini L, Figueiredo A, Fil A, Fontana M, Francesco M, Fuchs C, Futatani S, Gabellieri L, Gadariya D, Gahle D, Galassi D, Gałązka K, Galdon-Quiroga J, Galeani S, Gallart D, Gallo A, Galperti C, Garavaglia S, Garcia J, Garcia-Lopez J, Garcia-Muñoz M, Garzotti L, Gath J, Geiger B, Giacomelli L, Giannone L, Gibson S, Gil L, Giovannozzi E, Giruzzi G, Gobbin M, Gonzalez-Martin J, Goodman T, Gorini G, Gospodarczyk M, Granucci G, Grekov D, Grenfell G, Griener M, Groth M, Grover O, Gruca M, Gude A, Guimarais L, Gyergyek T, Hacek P, Hakola A, Ham C, Happel T, Harrison J, Havranek A, Hawke J, Henderson S, Hesslow L, Hitzler F, Hnat B, Hobirk J, Hoelzl M, Hogeweij D, Hopf C, Hoppe M, Horacek J, Hron M, Huang Z, Iantchenko A, Iglesias D, Igochine V, Innocente P, Ionita-Schrittwieser C, Isliker H, Ivanova-Stanik I, Jacobsen A, Jakubowski M, Janky F, Jardin A, Jaulmes F, Jensen T, Jonsson T, Kallenbach A, Kappatou A, Karpushov A, Kasilov S, Kazakov Y, Kazantzidis P, Keeling D, Kelemen M, Kendl A, Kernbichler W, Kirk A, Kocsis G, Komm M, Kong M, Korovin V, Koubiti M, Kovacic J, Krawczyk N, Krieger K, Kripner L, Křivská A, Kudlacek O, Kulyk Y, Kurki-Suonio T, Kwiatkowski R, Laggner F, Laguardia L, Lahtinen A, Lang P, Likonen J, Lipschultz B, Liu F, Lombroni R, Lorenzini R, Loschiavo V, Lunt T, Macusova E, Madsen J, Maggiora R, Maljaars B, Manas P, Mantica P, Mantsinen M, Manz P, Maraschek M, Marchenko V, Marchetto C, Mariani A, Marini C, Markovic T, Marrelli L, Martin P, Martín Solís A, Mastrostefano S, Matos F, Matthews G, Mayoral M L, Mazon D, Mazzotta C, Mc Carthy P, McClements K, McDermott R, Mcmillan B, Meineri C, Menkovski V, Meshcheriakov D, Messmer M, Micheletti D, Milanesio D, Militello F, Miron I, Mlynar J, Moiseenko V, Molina Cabrera P, Morales J, Moret

J M, Moro A, Moulton D, Nabais F, Naulin V, Naydenkova D, Nem R, Nespoli F, Newton S, Nielsen A, Nielsen S, Nikolaeva V, Nocente M, Nowak S, Oberkofler M, Ochoukov R, Ollus P, Olsen J, Omotani J, Ongena J, Orain F, Orsitto F, Paccagnella R, Palha A, Panaccione L, Panek R, Panjan M, Papp G, Paradela Perez I, Parra F, Passeri M, Pau A, Pautasso G, Pavlichenko R, Perek A, Pericoli Radolfini V, Pesamosca F, Peterka M, Petrzilka V, Piergotti V, Pigatto L, Piovesan P, Piron C, Piron L, Plyusnin V, Pokol G, Poli E, Pölöskei P, Popov T, Popovic Z, Pór G, Porte L, Pucella G, Puiatti M, Pütterich T, Rabinski M, Juul Rasmussen J, Rasmussen J, Rattá G, Ratynskaia S, Ravensbergen T, Réfy D, Reich M, Reimerdes H, Reimold F, Reiser D, Reux C, Reznik S, Ricci D, Rispoli N, Rivero-Rodriguez J, Rocchi G, Rodriguez-Ramos M, Romano A, Rosato J, Rubinacci G, Rubino G, Ryan D, Salewski M, Salmi A, Samaddar D, Sanchis-Sanchez L, Santos J, Särkimäki K, Sassano M, Sauter O, Scannell R, Scheffer M, Schneider B, Schneider P, Schrittwieser R, Schubert M, Seidl J, Seliunin E, Sharapov S, Sheeba R, Sias G, Sieglin B, Silva C, Sipilä S, Smith S, Snicker A, Solano E, Hansen S, Soria-Hoyo C, Sorokovoy E, Sozzi C, Sperduti A, Spizzo G, Spolaore M, Stejner M, Stipani L, Stober J, Strand P, Sun H, Suttrop W, Sytnykov D, Szepesi T, Tál B, Tala T, Tardini G, Tardocchi M, Teplukhina A, Terranova D, Testa D, Theiler C, Thorén E, Thornton A, Tilia B, Tolias P, Tomes M, Toscano-Jimenez M, Tsironis C, Tsui C, Tudisco O, Urban J, Valisa M, Vallar M, Vallejos Olivares P, Valovic M, Van Vugt D, Vanovac B, Varje J, Varju J, Varoutis S, Vartanian S, Vasilovici O, Vega J, Verdoolaege G, Verhaegh K, Vermare L, Vianello N, Vicente J, Viezzer E, Villone F, Voitsekhovitch I, Voltolina D, Vondracek P, Vu N, Walkden N, Wauters T, Weiland M, Weinzettl V, Wensing M, Wiesen S, Wiesenberger M, Wilkie G, Willensdorfer M, Wischmeier M, Wu K, Xiang L, Zagorski R, Zaloga D, Zanca P, Zaplotnik R, Zebrowski J, Zhang W, Zisis A, Zoletnik S and Zuin M 2019 *Nuclear Fusion* **59** 086020 ISSN 0029-5515, 1741-4326

[9] Snyder P, Groebner R, Hughes J, Osborne T, Beurskens M, Leonard A, Wilson H and Xu X 2011 *Nuclear Fusion* **51** 103016 ISSN 0029-5515, 1741-4326

[10] Mordijck S 2020 *Nuclear Fusion* **60** 082006 ISSN 0029-5515, 1741-4326

[11] Ham C J, Cowley S C, Brochard G and Wilson H R 2016 *Physical Review Letters* **116** 235001 ISSN 0031-9007, 1079-7114

[12] Huysmans G and Czarny O 2007 *Nuclear Fusion* **47** 659–666 ISSN 0029-5515, 1741-4326

[13] Cathey A, Hoelzl M, Lackner K, Huijsmans G, Dunne M G, Wolfrum E, Pamela S, Orain F and Günter S 2020 *Nuclear Fusion* ISSN 0029-5515, 1741-4326

[14] Laggner F, Diallo A, Cavedon M and Kolemen E 2019 *Nuclear Materials and Energy* **19** 479–486 ISSN 23521791

[15] Diallo A, Dominski J, Barada K, Knolker M, Kramer G J and McKee G 2018 *Physical Review Letters* **121** 235001 ISSN 0031-9007, 1079-7114

[16] Molina Cabrera P, Coda S, Porte L, Smolders A and TCV Team 2019 *Review of Scientific Instruments* **90** 123501 ISSN 0034-6748, 1089-7674

[17] Coda S, Agostini M, Albanese R, Alberti S, Alessi E, Allan S, Allcock J, Ambrosino R, Anand H, Andrèbe Y, Arnichand H, Auriemma F, Ayllon-Guerola J, Bagnato F, Ball J, Baquero-Ruiz M, Beletskii A, Bernert M, Bin W, Blanchard P, Blanken T, Boedo J, Bogar O, Bolzonella T, Bombarda F, Bonanomi N, Bouquey F, Bowman C, Brida D, Bucalossi J, Buermans J, Bufferand H, Buratti P, Calabró G, Calacci L, Camenen Y, Carnevale D, Carpanese F, Carr M, Carraro L, Casolari A, Causa F, Čeřovský J, Chellaï O, Chmielewski P, Choi D, Christen N, Ciraolo G, Cordaro L, Costea S, Cruz N, Czarnecka A, Dal Molin A, David P, Decker J, De Oliveira H, Douai D, Dreval M, Dudson B, Dunne M, Duval B, Eich T, Elmore S, Embréus O, Esposito B, Faitsch M, Farník M, Fasoli A, Fedorczak N, Felici F, Feng S, Feng X, Ferró G, Février O, Ficker O, Fil A, Fontana M, Frassinetti L, Furno I, Gahle D, Galassi D, Gałązka K, Gallo A, Galperti C, Garavaglia S, Garcia J, Garcia-Muñoz M, Garrido A, Garrido I,

Gath J, Geiger B, Giruzzi G, Gobbin M, Goodman T, Gorini G, Gospodarczyk M, Granucci G, Graves J, Gruca M, Gyergyek T, Hakola A, Happel T, Harrer G, Harrison J, Havlíčková E, Hawke J, Henderson S, Hennequin P, Hesslow L, Hogeweij D, Hogge J P, Hopf C, Hoppe M, Horáček J, Huang Z, Hubbard A, Iantchenko A, Igochine V, Innocente P, Ionita Schrittwieser C, Isliker H, Jacquier R, Jardin A, Kappatou A, Karpushov A, Kazantzidis P V, Keeling D, Kirneva N, Komm M, Kong M, Kovacic J, Krawczyk N, Kudlacek O, Kurki-Suonio T, Kwiatkowski R, Labit B, Lazzaro E, Linehan B, Lipschultz B, Llobet X, Lombroni R, Loschiavo V, Lunt T, Macusova E, Madsen J, Maljaars E, Mantica P, Maraschek M, Marchetto C, Marco A, Mariani A, Marini C, Martin Y, Matos F, Maurizio R, Mavkov B, Mazon D, McCarthy P, McDermott R, Menkovski V, Merle A, Meyer H, Micheletti D, Militello F, Mitosinkova K, Mlynář J, Moiseenko V, Molina Cabrera P, Morales J, Moret J M, Moro A, Mumgaard R, Naulin V, Nem R, Nespoli F, Nielsen A, Nielsen S, Nocente M, Nowak S, Offeddu N, Orsitto F, Paccagnella R, Palha A, Papp G, Pau A, Pavlichenko R, Perek A, Pericoli Ridolfini V, Pesamosca F, Piergotti V, Pigatto L, Piovesan P, Piron C, Plyusnin V, Poli E, Porte L, Pucella G, Puiatti M, Pütterich T, Rabinski M, Juul Rasmussen J, Ravensbergen T, Reich M, Reimerdes H, Reimold F, Reux C, Ricci D, Ricci P, Rispoli N, Rosato J, Saarelma S, Salewski M, Salmi A, Sauter O, Scheffer M, Schlatter C, Schneider B, Schrittwieser R, Sharapov S, Sheeba R, Sheikh U, Shousha R, Silva M, Sinha J, Sozzi C, Spolaore M, Stipani L, Strand P, Tala T, Tema Biwole A, Teplukhina A, Testa D, Theiler C, Thornton A, Tomaž G, Tomes M, Tran M, Tsironis C, Tsui C, Urban J, Valisa M, Vallar M, Van Vugt D, Vartanian S, Vasilovici O, Verhaegh K, Vermare L, Vianello N, Viezzer E, Vijvers W, Villone F, Voitsekhovitch I, Vu N, Walkden N, Wauters T, Weiland M, Weisen H, Wensing M, Wiesenberger M, Wilkie G, Wischmeier M, Wu K, Yoshida M, Zagorski R, Zanca P, Zebrowski J, Zisis A, Zuin M and the EUROfusion MST1 Team 2019 *Nuclear Fusion* **59** 112023 ISSN 0029-5515, 1741-4326

[18] Bravenec R V and Wootton A J 1995 *Review of Scientific Instruments* **66** 802–805 ISSN 0034-6748, 1089-7623

[19] Weisen H, Hofmann F, Dutch M J, Martin Y, Pochelon A, Moret J M, Duval B P, Hirt A, Lister J B, Nieswand C, Pitts R A, Pietrzyk Z A, Anton M, Behn R, Besson G, Bühlmann F, Chavan R, Fasel D, Favre A, Franke S, Isoz P, Lavanchy P, Joye B, Llobet X, Mandrin P, Marletaz B, Marmillod P, Magnin J C, Mayor J M, Paris P J, Perez A, Sauter O, van Toledo W, Tonetti G, Tran M Q, Troyon F and Ward D J 1996 *Plasma Physics and Controlled Fusion* **38** 1137–1148 ISSN 0741-3335, 1361-6587

[20] Pitzschke A, Behn R, Sauter O, Duval B P, Marki J, Porte L, Villard L, Medvedev S Y and the TCV Team 2012 *Plasma Physics and Controlled Fusion* **54** 015007 ISSN 0741-3335, 1361-6587

[21] Sheikh U, Dunne M, Frassinetti L, Labit B, Blanchard P, Duval B, Février O, Galassi D, Merle A, Reimerdes H and Theiler C 2021 *Nuclear Materials and Energy* **26** 100933 ISSN 23521791

[22] Sheikh U A, Dunne M, Frassinetti L, Blanchard P, Duval B P, Labit B, Merle A, Sauter O, Theiler C, Tsui C, the TCV Team and the EUROfusion MST1 Team 2019 *Plasma Physics and Controlled Fusion* **61** 014002 ISSN 0741-3335, 1361-6587

[23] Wilson H 2010 *Fusion Science and Technology* **57** 174–182 ISSN 1536-1055, 1943-7641

[24] Hutchinson I H 2002 *Principles of Plasma Diagnostics* 2nd ed (Cambridge University Press) ISBN 978-0-521-80389-2 978-0-521-67574-1 978-0-511-61363-0

[25] Laviron C, Donné A J H, Manso M E and Sanchez J 1996 *Plasma Physics and Controlled Fusion* **38** 905–936 ISSN 0741-3335, 1361-6587

[26] Varela P, Manso M E, Silva A, Fernandes J and Silva F 1995 *Review of Scientific Instruments* **66** 4937–4942 ISSN 0034-6748, 1089-7623

[27] Mazzucato E 1998 *Review of Scientific Instruments* **69** 2201–2217 ISSN 0034-6748, 1089-7623

[28] Shevchenko V F, Petrov A A and Petrov V G 1993 *International Journal of Infrared and Millimeter Waves* **14** 1755–1768 ISSN 0195-9271, 1572-9559

[29] Heijnen S 1995 *Pulsed-Radar Reflectometry: A New Approach to Measure Electron Densities in Thermonuclear Plasmas* Ph.D. thesis Universiteit Utrecht FOM-instituut voor plasmafysica

[30] Molina Cabrera P A 2019 *Tokamak Plasma Edge Studies by Microwave Short-Pulse Reflectometry and Backscattering* Ph.D. thesis Ecole Polytechnique Federale de Lausanne Lausanne, Switzerland

[31] Clairet F, Bottereau C, Medvedeva A, Molina D, Conway G D, Silva A, Stroth U, ASDEX Upgrade Team, Tore Supra Team and EUROfusion MST1 Team 2017 *Review of Scientific Instruments* **88** 113506 ISSN 0034-6748, 1089-7623

[32] Becker W 2019 *The Bh TCSPC Technique - Principles and Applications* two thousand, nineteenth ed (Berlin, Germany: Becker & Hickl GmbH)

[33] Doyle E J, Kim K W, Lee J H, Peebles W A, Rettig C L, Rhodes T L and Snider R T 1996 Reflectometry Applications to ITER *Diagnostics for Experimental Thermonuclear Fusion Reactors* ed Stott P E, Gorini G and Sindoni E (Boston, MA: Springer US) pp 117–132 ISBN 978-1-4613-8020-7 978-1-4613-0369-5

[34] Biglari H, Diamond P H and Terry P W 1990 *Physics of Fluids B: Plasma Physics* **2** 1–4 ISSN 0899-8221

[35] Goodman T, Alberti S, Henderson M, Pochelon A and Tran M 1997 Design and installation of the electron cyclotron wave system for the TCV tokamak. *Fusion Technology 1996* (Elsevier) pp 565–568 ISBN 978-0-444-82762-3

[36] Silva M, Goodman T, Felici F and Porte L 2011 *Fusion Engineering and Design* **86** 1256–1259 ISSN 09203796

[37] Doane J L 1982 *International Journal of Electronics* **53** 573–585 ISSN 0020-7217, 1362-3060

[38] Molina Cabrera P, Coda S, Porte L, Offeddu N, Lavanchy P, Silva M, Toussaint M and TCV Team 2018 *Review of Scientific Instruments* **89** 083503 ISSN 0034-6748, 1089-7623

[39] Vianello N, Tsui C, Theiler C, Allan S, Boedo J, Labit B, Reimerdes H, Verhaegh K, Vijvers W, Walkden N, Costea S, Kovacic J, Ionita C, Naulin V, Nielsen A, Juul Rasmussen J, Schneider B, Schrittwieser R, Spolaore M, Carralero D, Madsen J, Lipschultz B, Militello F, The TCV Team and The EUROfusion MST1 Team 2017 *Nuclear Fusion* **57** 116014 ISSN 0029-5515, 1741-4326

[40] Moret J M, Duval B, Le H, Coda S, Felici F and Reimerdes H 2015 *Fusion Engineering and Design* **91** 1–15 ISSN 09203796

[41] Taboga M 2017 *Lectures on Probability Theory and Mathematical Statistics* ISBN 978-1-981369-19-5

[42] Conway G D 1993 *Review of Scientific Instruments* **64** 2782–2788 ISSN 0034-6748, 1089-7623

[43] Groebner R J and Osborne T H 1998 *Physics of Plasmas* **5** 1800–1806 ISSN 1070-664X, 1089-7674

[44] Transport I P E G o C, Database I P E G o C and Editors I P B 1999 *Nuclear Fusion* **39** 2175–2249 ISSN 0029-5515

[45] Greenwald M 2002 *Plasma Physics and Controlled Fusion* **44** R27–R53 ISSN 07413335

[46] Pitzschke A 2010 *Pedestal Characteristics and MHD Stability of H-Mode Plasmas in TCV* Ph.D. thesis Ecole Polytechnique Federale de Lausanne Lausanne, Switzerland

[47] Hennequin P 2007 Inter-ELM fluctuations and flows and their evolution when approaching the density limit in the ASDEX Upgrade tokamak *44th EPS Conference on Plasma Physics* vol P1.167 (Belfast, UK)

[48] Moret J M, Buhlmann F and Tonetti G 2003 *Review of Scientific Instruments* **74** 4634–4643 ISSN 0034-6748, 1089-7623

[49] Nunes I, Manso M, Serra F, Horton L, Conway G, Loarte A and Teams t A U a C R 2005 *Nuclear Fusion* **45** 1550–1556 ISSN 0029-5515, 1741-4326

[50] Reimerdes H, Pochelon A and Suttrop W 1998 *Nuclear Fusion* **38** 319–323 ISSN 0029-5515